

Energy-Autonomous, Flexible, and Transparent Tactile Skin

Carlos García Núñez, William Taube Navaraj, Emre O. Polat, and Ravinder Dahiya*

Tactile or electronic skin is needed to provide critical haptic perception to robots and amputees, as well as in wearable electronics for health monitoring and wellness applications. Energy autonomy of skin is a critical feature that would enable better portability and longer operation times. This study shows a novel structure, consisting of a transparent tactile sensitive layer based on single-layer graphene, and a photovoltaic cell underneath as a building block for energy-autonomous, flexible, and tactile skin. Transparency of the touch sensitive layer is considered a key feature to allow the photovoltaic cell to effectively harvest light. Moreover, ultralow power consumed by the sensitive layer (20 nW cm^{-2}) further reduces the photovoltaic area required to drive the tactile skin. In addition to its energy autonomy, the fabricated skin is sensitive to touch, mainly because a transparent polymeric protective layer, spin-coated on the sensor's active area, makes the coplanar capacitor sensitive to touch, detecting minimum pressures of 0.11 kPa with a uniform sensitivity of 4.3 Pa^{-1} along a broad pressure range. Finally, the tactile skin patches are integrated on a prosthetic hand, and the responses of the sensors for static and dynamic stimuli are evaluated by performing tasks, ranging from simple touching to grabbing of soft objects.

such as diabetes. To satisfy the requirements of such a system, active materials with intrinsic properties, including good mechanical, electrical, optical, and structural properties, are in high demand.^[1]

The development of suitable flexible pressure sensors for e-skin applications has been a challenge, due to inadequate flexibility, conductivity, large-area manufacturability, and reliable and repeatable performance of the structure, to be applicable in practical robots.^[7] In this regard, only very few approaches have been successfully employed in actual robots.^[7,8] Further, making the e-skin transparent adds an extra dimension in the functional design space of e-skin, as it enables incorporating photovoltaic (PV)-energy harvesting, electro/thermochromicity, chameleon effect, etc. Along with a new generation of flexible and stretchable solar cells,^[9] this will allow fabrication of energy-autonomous, stretchable e-skins.

Accordingly, a novel approach is explored in this work, of a vertical-layered-stack structure consisting of a photovoltaic cell attached to the back plane of a transparent tactile skin; where skin transparency is a crucial feature that allows light to pass through, making the building block unique and opening a new, promising line of energy-autonomous devices for flexible electronics. In this regard, graphene is a promising material as it offers key parameters to develop nonplanar, transparent electronic or tactile skin. It has been shown that graphene has a good combination of stiffness ($\approx 1000 \text{ GPa}$) and tensile strength ($\approx 100 \text{ GPa}$).^[10] Together with its sunlight blindness^[11] and good electrical conductivity,^[12] graphene has also emerged as a viable candidate for various flexible, transparent electronic and optoelectronic devices.^[13–16] Moreover, in our recent work, we demonstrated that high-quality graphene can be synthesized and transferred on large area, flexible substrates (400 cm^2) with a very low-cost and easy fabrication process.^[15] Owing to the intrinsic properties and advances in the synthesis and fabrication of devices, graphene is also a promising candidate for the development of high-performance e-skin, requiring large area device fabrication on nonplanar surfaces.

A few flexible pressure sensors reported in literature, based on capacitive,^[17–20] piezoelectric,^[21] and piezoresistive sensing mechanisms,^[2,22–28] use graphene as an active material. Piezoresistive sensors transduce the pressure imposed on the sensor's active area in terms of resistance change, and offer an attractive solution for pressure sensing due to advantages such as low cost and easy signal collection. Graphene-based piezoresistive pressure sensors have been reported in various configurations. For example, Yao et al. demonstrated the fabrication of flexible pressure sensors based on a graphene nanosheet on

1. Introduction

Human skin is composed of countless neural sensors that can perceive various stimuli, such as pressure, temperature, and texture of an object. In addition to its advanced sensing capability, our skin is mechanically flexible, stretchable, robust, and self-healing. A tactile or electronic skin (e-skin) is an artificial smart skin, aiming to provide similar sense of touch to robots and artificial prostheses by mimicking some of the features of human skin.^[1–5] In this regard, there is a need to develop and integrate multiple sensors on nonplanar, flexible, and conformal surfaces, first, to make it viable, and then, to advance today's e-skin applications.^[6] For example, a flexible, transparent skin provided with touch/pressure sensors will allow robots to detect the strength and location of the pressure exerted on the skin surface. Similarly, with a different set of sensors the e-skin could also act as a second skin, allowing us to detect chronic diseases

Dr. C. G. Núñez, W. T. Navaraj, Dr. E. O. Polat,
Dr. R. Dahiya
School of Engineering
University of Glasgow
G12 8QQ Glasgow, UK
E-mail: ravinder.dahiya@glasgow.ac.uk



This is an open access article under the terms of the Creative Commons Attribution License, which permits use, distribution and reproduction in any medium, provided the original work is properly cited.

The copyright line of this paper was changed 26 May 2017 after initial publication.

DOI: 10.1002/adfm.201606287

Table 1. Characteristics of pressure sensors.

	This work	Bao and co-workers ^[19]	Ho et al. ^[20]	Yao et al. ^[22]	Zhu et al. ^[29]	Tian et al. ^[23]
Material	Single-layer graphene	Structured PDMS	Graphene	Graphene nanosheets	Reduced graphene oxide	Laser-scribed graphene
Structure	Coplanar interdigitated electrodes	Parallel electrodes	Parallel electrodes	Conductive sponge	Microstructure polymer	Foam-like structure
Sensor type	Capacitive	Capacitive	Capacitive	Piezoresistive	Piezoresistive	Piezoresistive
Sensitivity [kPa ⁻¹]	0.01	0.55	0.002	0.26	5.50	0.96
Pressure range [kPa]	<80	<2	<500	<10	<0.1	<100
Min. pressure [kPa]	0.11	0.003	0.5	0.009	0.0015	5

polyurethane (PU) sponge.^[22] The use of graphene nanosheets as a conductive coating on commercial PU sponge results in a high contact-area of the conductive sponge, and improves the sensitivity of the sensor (0.26 kPa⁻¹) in low-pressure regimes (<2 kPa). However, the thick and nontransparent sponge-like structure is a bottleneck when it comes to system integration on transparent e-skin. Following a similar approach, Zhu et al. used polydimethylsiloxane (PDMS) films with pyramid microstructures as a substrate for the deposition of reduced graphene oxide (rGO) layers, resulting in microstructured rGO that demonstrated ultrahigh sensitivity to pressure.^[29] The anisotropic pyramid-microstructures-based rGO-arrays not only endowed the pressure sensor with high sensitivity of 5.5 kPa⁻¹ (<100 Pa) at low detection limits of 1.5 Pa, but also presented fast response times of 0.2 ms. However, the sensitivity of these sensors drops significantly at pressures above 5 kPa, which is a drawback when it comes to daily tasks where normal manipulation, such as human object grabbing, involves forces in the range of 15–90 gm wt, and 90% of the mechanoreceptors can detect pressures as low as 8.5 kPa.^[30] Considering involvement of tactile sensors in various exploratory tasks in robotics and prosthetic applications, a pressure sensitivity range of 1–1000 kPa and a dynamic range of 1:1000 are desirable. In this regard, the use of a foam-like structure based on laser-scribed graphene demonstrates sensitivities of the piezoresistive pressure sensor up to 0.96 kPa⁻¹ in a wide pressure regime (0–50 kPa).^[23]

As mentioned above, graphene pressure sensors can also be based on a capacitive mechanism.^[17–20] Capacitive pressure sensors typically consist of two parallel plates separated with a soft dielectric material. The pressure applied normal to the sensor surface squeezes the material and reduces the gap between parallel plates, leading to a change of the measured capacitance. In this regard, Bao et al. fabricated a flexible pressure-capacitive sensor array based on PDMS film sandwiched between two plastic substrates, each of which contained a set of conductive lines serving as an address and data lines.^[19] The use of microstructured PDMS showed a maximum sensitivity of 0.55 kPa⁻¹, which is around 35 times higher than the sensitivity of unstructured PDMS in the same range of pressures. Moreover, by using the 6 × 6 μm² pyramid-structured PDMS as a dielectric layer on organic field effect transistors, they could detect ultra-small weights of about 20 mg from the capacitance change. Similarly, Ho et al. reported transparent graphene oxide and rGO-based multifunctional e-skin, with humidity, thermal, and pressure sensors in a 3D structure.^[20] However, encapsulation of the pressure sensors in this 3D stacked structure appears to

hinder the sensor performance, which shows a low sensitivity of 0.002 kPa⁻¹ at pressures up to 450 kPa. A comparison of the above pressure sensors with the pressure sensors developed in this work, in terms of their composition (material and structure), mechanism, and output characteristics (sensitivity, pressure range, and minimum pressure), etc., is given in **Table 1**.

Here, we present a transparent tactile e-skin based on single-layer graphene, coplanar interdigitated capacitive (IDC) electrodes. The interdigitated structure of presented sensors also allows the tactile skin to be flexible and, additionally, is a promising structure for the development of near-future, stretchable tactile skins. We demonstrate the feasibility of large-scale and low-cost dry fabrication of a flexible and transparent e-skin for pressure sensing and tactile mapping. We improve the functionality of the e-skin by reading outputs of graphene sensors using commercial off-the-shelf chip, which is a promising approach to make robotic hands sensitive to their surroundings. This can be further extended to make crucial contributions to human prosthetics, augmenting human sensing when fashioned into clothing. Furthermore, we demonstrate the integration of transparent pressure sensors directly on top of a solar cell, as a step toward energy-autonomous e-skin.

2. Results and Discussion

2.1. Graphene on Transparent Flexible Substrates

We started with the fabrication of a touch-sensitive layer by large-area transfer of graphene on 125-μm-thick, flexible poly vinyl chloride (PVC) substrates. **Figure 1A–C** shows the transfer printing of large area chemical vapor deposited (CVD) graphene on flexible PVC substrates using a hot lamination process.^[31]

In this work, we used commercially available single-layer graphene CVD grown on Cu, of which the growth parameters and the characterization on rigid substrates have been previously demonstrated elsewhere.^[32–34] We analyzed some of the properties of graphene layers on flexible PVC substrates after transfer printing. First, electrical properties of graphene were analyzed by a transfer-length method (TLM) (see the Experimental Section). Both the sheet resistance (R_s) of graphene-on-PVC and contact resistance (R_c) between graphene and Ti/Au electrodes were measured by the TLM. **Figure 1D** shows the measured total resistance (R_T) of samples with different L_c (the inset of **Figure 1D** shows photographs of graphene-on-PVC

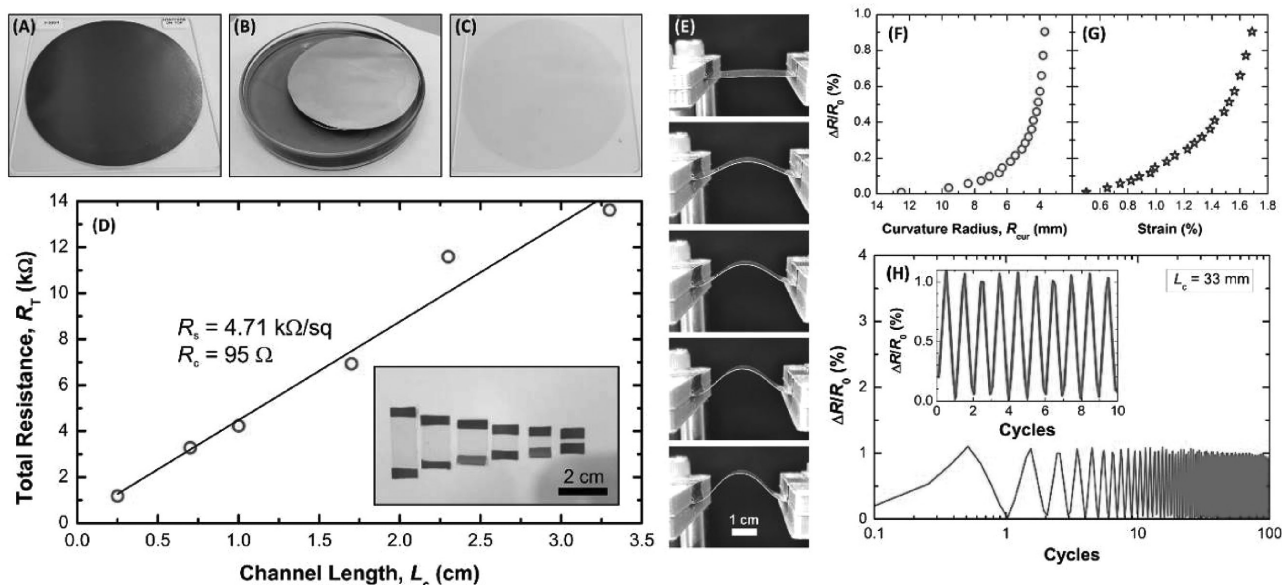


Figure 1. Electromechanical characterization of flexible graphene-on-PVC substrates. A) Commercially available CVD graphene on 4 in. Cu foil. B) Wet-etching of PVC laminated Cu in 1 M FeCl₃ solution. C) Resultant graphene-on-PVC after etching of Cu foil. D) Total resistance (R_T) of graphene-on-PVC versus channel length (L_c); inset: graphene films with various L_c . E) Snapshots of bending experiment carried out on a 33-mm-channel-length sample. $\Delta R/R_0$ versus F) R_{cur} and G) strain. H) Cyclic bending test representing $\Delta R/R_0$ versus bending cycles; inset: zoom-in of the first ten cycles.

samples with various L_c) and represents the experimental data with the best linear fitting. Using the slope (R_s/L_c) and the y-intercept ($2R_c$) of the fitted line represented in Figure 1D, the values of R_s and R_c calculated from the total resistance formula, $R_T = (R_s/W_c)L_c + 2R_c$, are 4.71 k Ω sq⁻¹ and 95 Ω , respectively.

To analyze the electromechanical properties and cyclic stability of the graphene-on-PVC samples, we applied mechanical stress through a bending test and recorded the resistance change. Accordingly, the active bending test of the flexible graphene-on-PVC sample with an L_c of 33 mm was carried out taking snapshots while measuring R_T every 0.2 mm, up to a step size of 4 mm. Figure 1E shows a reduced sequence of snapshots, including step sizes of, from the top to the bottom of the figure, 0, 1, 2, 3, and 4 mm. The resistance change ($\Delta R/R_0$) as a function of both the radius of curvature (R_{cur}) and the strain are shown in Figure 1F,G, respectively. The latter was calculated by^[6,35,36]

$$\text{Strain (\%)} = \frac{F(t_s + t_f)}{2R_c} \quad (1)$$

where t_s and t_f are the thickness of the substrate and the film (graphene), respectively, and F is a parameter that depends on both the thickness (t_f/t_s) and Young's modulus (Y_f/Y_s) ratios of the substrate and the film. Due to the 2D nature of graphene, $t_s \gg t_f$; thus, from Equation (1) we can assume that F is ≈ 1 . From Figure 1F it can be deduced that $\Delta R/R_0$ reaches a maximum value of around 0.92% when the graphene layer is bent up to $R_{cur} = 4$ mm, which corresponds to a strain of around 1.7% (Figure 1G). To demonstrate the stability of the graphene films, we also performed a cyclic bending test with 100 cycles. Figure 1H shows the resultant study, observing $\Delta R/R_0$ values lower than 1%, along with the entire range, which is a good

indication of the materials stability under dynamic bending. We believe the observed changes in resistance are mainly dominated by the change of R_c due to the crack formation at the graphene–Au interface.

2.2. Fabrication of Graphene-Based Transparent Touch-Sensitive Layer

After electromechanical characterisation of graphene-on-PVC samples, they were used to fabricate flexible capacitive touch sensors. Figure 2 summarizes the fabrication steps of graphene-based, transparent, and flexible capacitive touch sensors (see further details in the Experimental Section). Figure 2A presents the hot lamination method for transfer printing of CVD graphene to 125- μ m-thick PVC substrates. At 110 $^\circ$ C, the active side of the PVC sticks to the graphene holding Cu and makes a conformal contact to the Cu surface. Etching the Cu foil in FeCl₃ solution yields the graphene-on-PVC samples (Figure 2B). Using electron beam (e-beam) evaporation and a shadow mask, we deposited Ti/Au (10 nm/100 nm) on the edges of the sample, to obtain electrical contact pads (Figure 2C). After this, we used a computer-controlled cutting machine, equipped with a plotter blade, to shape the single-layer graphene as coplanar interdigitated electrodes (Figure 2D). The cutting machine allowed us to create various patterns without using complex lithographic and chemical procedures. Following the patterning step, we spin-coated and cured 25- μ m-thick PDMS on a graphene channel. The PDMS serves as the protective dielectric layer between external stimuli and graphene, and also provides a good encapsulation of the device (Figure 2E). Figure 2F presents the resultant transparent and flexible touch/pressure sensor that is eventually integrated on a robotic hand.

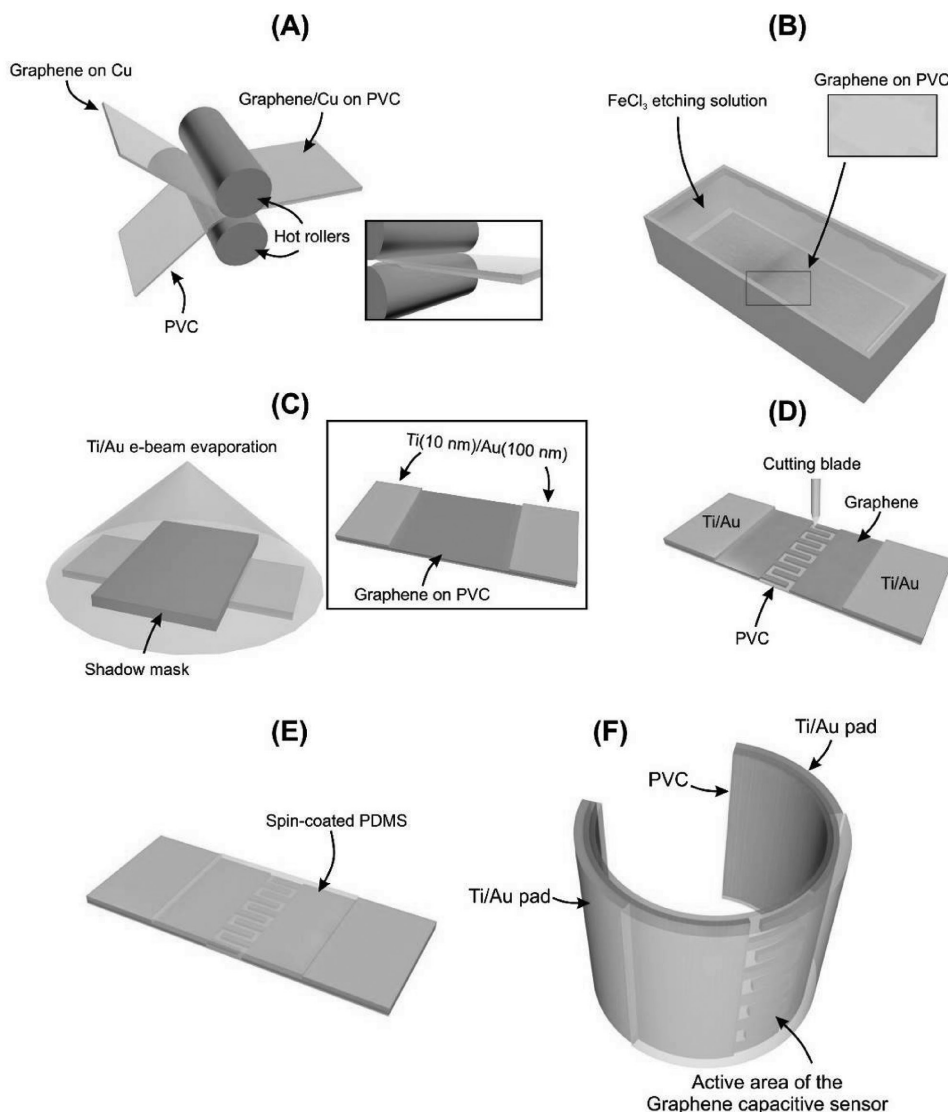


Figure 2. Schematic illustration showing the fabrication steps of graphene-based flexible capacitive touch sensors. A) Hot lamination transfer printing of CVD graphene on PVC flexible substrate. B) Graphene-on-PVC sample after etching the seed metal, i.e., Cu. C) Au deposition via e-beam evaporation through shadow mask. D) Patterning of graphene channel with an electronic cutting tool. E) Flexible capacitive touch sensor after spin-coating and curing of PDMS protective layer. F) Resultant graphene-based capacitive touch sensor.

Figure 3A shows the high flexibility of the fabricated graphene-on-PVC samples with an interdigitated pattern on it. Figure 3B shows various flexible sensing devices with Ti/Au electrical contact pads. As shown in Figure 3D, by using a computer-controlled cutting system we developed sensors with different interdigitated designs on graphene (e.g., linear or meander), which allowed us to tune the electrode geometry to improve the device sensitivity through the increase of the sensor active area. In this work, we have compared the sensing response of touch sensors with different sensing areas, i.e., the area of the gap between electrodes, comprising 11.25 mm^2 (vertical lines, Figure 3B, top), 13.45 mm^2 (horizontal lines, Figure 3B, middle), and 14.55 mm^2 (squared shape meanders, Figure 3B, bottom). As shown in Section F of the Supporting Information, squared shape meanders are the geometry that exhibits the maximum capacitance response, along

with a wide range of pressures. For that reason, that will be the geometry of the sensors used for the development of the tactile skin. Figure 3C presents the optical microscope image of the cuts on graphene-on-PVC sample. The depth of the cut can be arranged for various substrate thicknesses by using the software (Figure S1, Supporting Information). Figure 3D shows a magnified optical microscope image and the dashed line indicates the scanning direction of stylus profiler. Here, we performed $\approx 25 \text{ }\mu\text{m}$ deep cutting for $125\text{-}\mu\text{m}$ -thick PVC substrates, to isolate graphene layers without compromising the overall mechanical robustness of the structure (Figure 3E). However, lateral and vertical resolution of this method is highly dependent on the material under cutting. Using the specific cutting parameters described in the Supporting Information, this shows lateral resolution down to $50 \text{ }\mu\text{m}$ and depths around $25 \text{ }\mu\text{m}$. The cutting process also creates a stress on the flexible

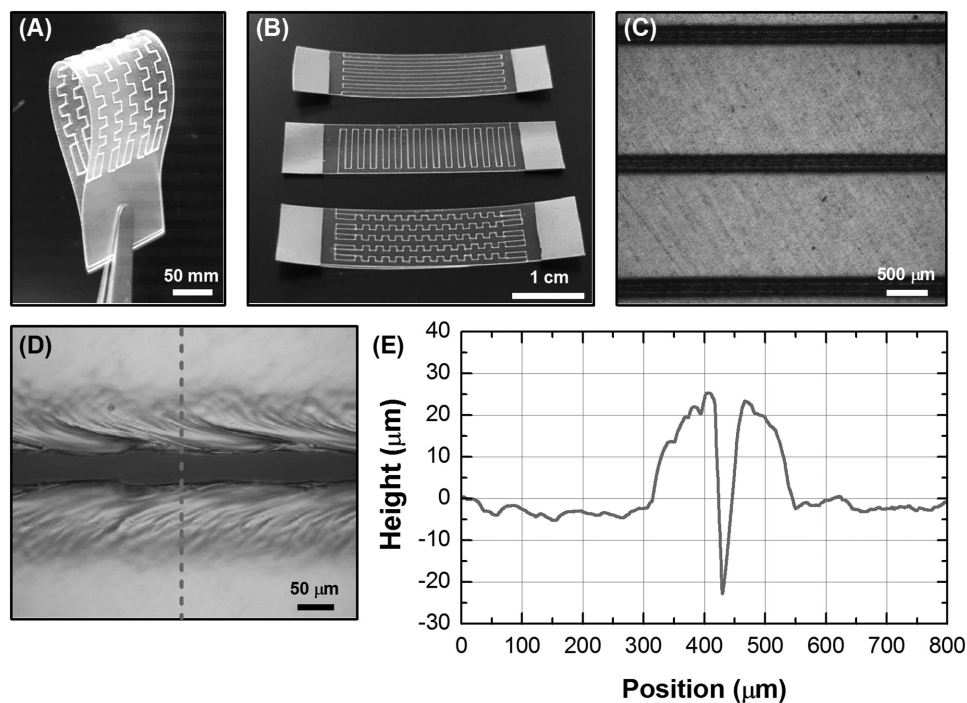


Figure 3. Graphene based flexible capacitive sensors with various interdigitated patterns. A) Flexible graphene-on-PVC sample with an interdigitated pattern. B) Photograph of graphene-based flexible capacitive touch sensors with different geometries of interdigitated electrodes. C) Optical microscope image of the longitudinal cuts and D) its corresponding magnified image. E) Profile of the cut measured with stylus profiler along the dashed line in (D).

substrates, which results in $\approx 20\text{-}\mu\text{m}$ -thick material accumulation on the edges of the cuts. Since fabricated sensors are based on large-area graphene electrodes, the resulting material accumulation at the edges of the defined gap has negligible effects on the mechanical properties and performance of sensors. To the best of our knowledge, we present here for the first time a low-cost dry method to fabricate coplanar interdigitated electrodes based on single-layer graphene. The presented dry fabrication method introduces features such as reliability, amenability, upward scalability, and low cost, which are attractive advantages with respect to other techniques conventionally used to define patterns on graphene, that present drawbacks comprising graphene under-etching and contamination from the contacting mask (mask lithography),^[37] undesirable presence of residual polymers that contaminate the graphene surface (photolithography),^[38] low fabrication yield and harmful effects on atomically thick graphene layers (laser cutting),^[39,40] and complex and costly techniques, incompatible with plastic substrates (laser scribing and helium ion microscopy).^[38,39]

2.3. Static and Dynamic Response of Touch Sensors

After the fabrication of graphene-based, flexible capacitive touch sensors, we studied their response under quasi-static touching conditions. Using a Keysight (E4980AL) LCR meter, we first measured the base capacitance (C_0) of sensors in air ambient conditions and typically obtained values in the range of $\approx 8\text{--}9$ pF. C_0 was also measured before the deposition of the PDMS protection layer (see PDMS deposition conditions in the

Supporting Information: Section B), showing a value of 5.5 pF. This shows that the PDMS protective layer increases the sensor capacitance, which is largely due to the higher dielectric constant of PDMS with respect to the air ($\epsilon = 3\epsilon_0$, with ϵ_0 being the dielectric constant of the air). We also noted that the thickness of PDMS strongly influences the C_0 , i.e., the thicker the PDMS, the lower the C_0 (Figure S2, Supporting Information). In addition to the PDMS protective layer, the thickness and material of the substrate contribute to the total sensor capacitance.

For the sake of comparison, we have analyzed the response of graphene capacitive sensors to the touch, using both conductive and insulating probes, consisting of 1-mm-thick PDMS coated with a 500-nm-thick Au layer, and 1-mm-thick PDMS without an Au layer, respectively (Figure S3, Supporting Information). Both conductive and insulating probes cause an increase in the capacitance of sensors with respect to C_0 . Comparing both results (Figure S4, Supporting Information), the conductive PDMS rubber can produce higher responses in the capacitance change (e.g., $\Delta C/C_0 = 25\%$ at 40 kPa) than its insulating counterpart (e.g., $\Delta C/C_0 = 10\%$ at 40 kPa). These results are mainly due to two main mechanisms: 1) the change of the PDMS protective layer thickness due to deformation and 2) the existence of a third capacitance coming from the touching probe. The first mechanism is observed in both experiments utilizing conductive and insulating PDMS rubbers, and it is in good agreement with the variation of sensor capacitance with PDMS thickness (Figure S2, Supporting Information). The second mechanism is only appreciable in the case of using a conductive PDMS rubber, playing the role of a third electrode that adds an additional capacitance to the total capacitance of

the sensor (Figure S5, Supporting Information). While the response obtained from conductive and insulator probes can be calibrated to read an accurate pressure independently on the probe, the demonstrated touch selectivity of the sensors increases e-skin functionality and would allow the spatial detection of objects with different compositions in contact with the e-skin. To analyze thoroughly this experimental evidence, we carried out quasi-static touching experiments by using a linear stage motor to exert periodic pulses of pressure on the device active area (Figure 4A). As mentioned above, for gentle touching we attached the described insulating PDMS rubber to the stage. Using LabVIEW software, the linear stage movement was configured to perform quasi-static touching experiments, consisting of squared-shape pulses of pressure with a frequency of 2 Hz. Figure 4B represents the capacitive response ($\Delta C/C_0$) measured over time on graphene-based, flexible capacitive touch sensors. The high accuracy of the linear stage motor enables us to move the PDMS rubber down to micrometric distances and allows us to exert periodic pressures of different magnitudes on the sensors. In this regard, we exerted controlled external pressures on the sensors overtime and simultaneously recorded the capacitance change with the LCR meter (Figure 4B). First, we calibrated the pressure exerted on sensors as a function of the linear stage step length using a commercial force meter (Figure S6, Supporting Information). Figure 4B shows a collection of five different measurements consisting

of ten periodic touching cycles (frequency of 0.42 Hz) carried out at different pressures ranging between 9.8 and 72.1 kPa; these measurements were carried out following different routines, i.e., from low to high pressures and vice versa, to analyze possible hysteresis effects of the PDMS protective layer. All sensors based on interdigitated electrodes with different geometries, including lines and meandered shapes, were analyzed (Figure 3B). Among various geometries, the meandered-shaped interdigitated electrodes (Figure 3A) provided one of the highest capacitance modulations and uniform responses, along with the scanned pressure range (Figure S7, Supporting Information). Following these findings, we further analyzed the response of this specific sensor sample. This capacitive sensor shows stable response for all the analyzed pressures, i.e., pressures of 9.8, 26.7, 47.3, 64.6, and 72.4 kPa, resulting in $\Delta C/C_0$ of 1.9%, 10.5%, 17.3%, 25.5%, and 53.1%, respectively, independently of the measurement routine, i.e., from low to high pressures, or vice versa. This result can be explained by arguing that the thin thickness of the PDMS reduces the stretching/releasing process period during and after the pressure is applied on the sensor. More importantly, $\Delta C/C_0$ presents different values depending on the applied pressure. This pressure sensitivity is a novel and interesting behavior in coplanar based structures, especially because the conventional coplanar or staggered structures (coplanar capacitor type I in Figure 4C) commonly used in commercial capacitive touch screens can

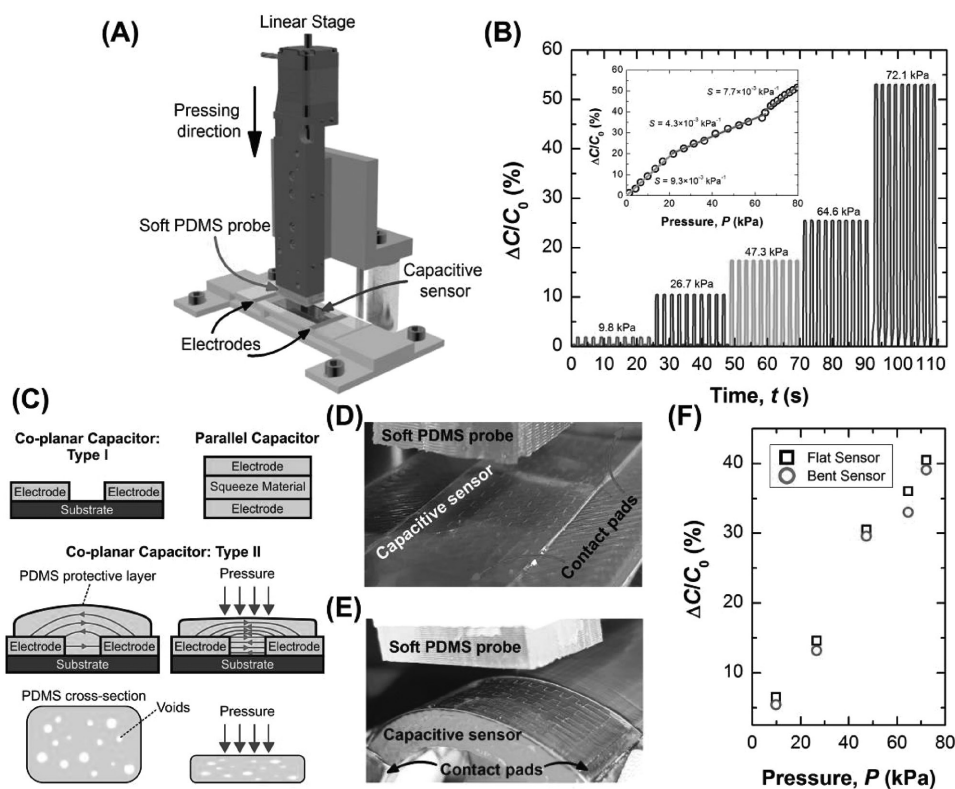


Figure 4. Capacitive response of graphene-based flexible sensors. A) 3D schematic illustration of experimental setup. B) Response of the graphene-based flexible sensor under the quasi-static application of pressure overtime for various pressures; inset: extracted sensitivities for a wide pressure regime. C) Coplanar- and parallel-based capacitors; type I capacitor is sensitive to touch and proximity, whereas type II and parallel capacitors are sensitive to pressure. D,E) Photographs of capacitive sensors under test in flat and bending conditions. F) $\Delta C/C_0$ versus pressure measured at D) flat and E) bending conditions.

only sense the presence or absence of touch. Other common approaches reported for graphene capacitive sensors is the use of graphene as two conductive parallel electrodes separated with a stretchable material (parallel capacitor in Figure 4C).^[17,18] In this approach, the graphene directly experiences the pressure, which may damage the graphene and may lead to reliability issues. The coplanar structure presented here (type II in Figure 4C) shows an additional feature compared to type I, i.e., the sensitivity to the pressure. The origin of their pressure sensitivity is mainly attributed to the change of the PDMS dielectric constant under compression. The cured PDMS has a porous structure^[41,42] and the volumetric density of voids in PDMS decreases (Figure 4C) when it is pressed. This leads to a change in its effective dielectric constant and thus the measured capacitance.

The sensitivity of the sensor was calculated by $S = \delta(\Delta C/C_0)/\delta P$, where P is the applied pressure. S depends on the applied pressure range, as clearly observed in the inset of Figure 4B. From 0 to 20 kPa, sensors present a sensitivity of $9.3 \times 10^{-3} \text{ kPa}^{-1}$; between 20 and 60 kPa they show $4.3 \times 10^{-3} \text{ kPa}^{-1}$; and at pressures higher than 60 kPa, sensors present a sensitivity of $7.7 \times 10^{-3} \text{ kPa}^{-1}$. Capacitive sensors fabricated in this work present S lower than those obtained in capacitive sensors based on conductive porous sponges that show up to 0.26 kPa^{-1} in a range of pressures below 2 kPa. In contrast, our sensors show similar sensitivities along with a wider range of pressures up to 80 kPa, and have attractive properties, such as transparency, thin structure, and sensitivity to pressure, which are all promising features for e-skin applications. In addition, the sensor developed in this work shows a unique behavior that has not been observed before, which is the second increase of the sensitivity above 60 kPa. That behavior makes this device even more attractive in a broad range of pressures, where other

reported pressure sensors show loss of sensitivity with pressure (Figure S8 and Table S1, Supporting Information).

In order to evaluate the functionality of the graphene capacitive touch sensors, especially when they are integrated nonplanar surfaces, we compared the measured response of sensors on both flat (Figure 4D) and nonplanar surfaces (Figure 4E). Quasi-static measurements of $\Delta C/C_0$ were carried out in a flat and bending mode, using flat and bent PDMS soft probes to touch the same active area in both scenarios (Figure S9, Supporting Information). Figure 4F shows that the response, i.e., $\Delta C/C_0$, of the sensors remains unaffected in both cases. This is mainly because of the intrinsic mechanical robustness of graphene, which preserves electrical properties after transfer to either flat or nonplanar surfaces. In addition, there is good conformal contact formed between graphene and the PVC substrate during the hot lamination transfer procedure (Figure 2A), making the device architecture more robust and very stable, even under the stresses experienced during bending.

2.4. Tactile e-Skin on Artificial Limb

To check the validity of the graphene touch sensors for e-skin, the sensors were integrated at the intermediate and proximal phalanges of an i-Limb—a state-of-the-art bionic hand (Figure 5A). Due to the different size of the phalanges, sensors placed at intermediate phalanges have less active area than those placed at proximal phalanges. Figure 5A shows a magnified image of sensors on each phalange, with clearly visible IDC electrodes. The response of graphene sensors was converted from capacitive variation to a voltage through a readout interface circuitry that was designed and implemented in a flexible polyimide substrate (Figure S10, Supporting Information). The

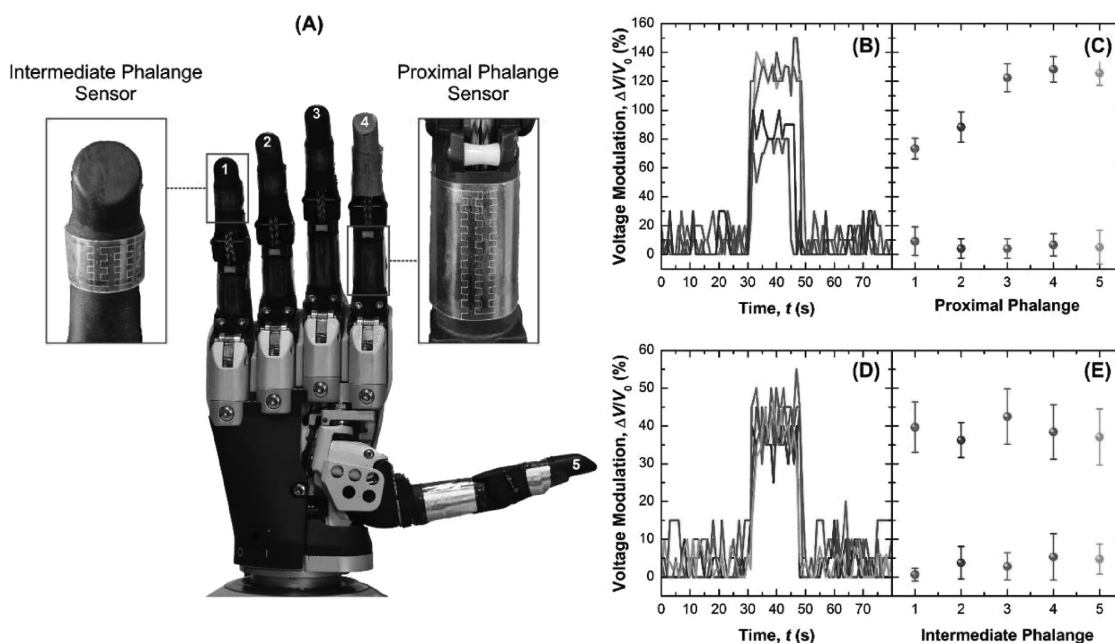


Figure 5. Static characterization of graphene touch sensors. A) Graphene capacitive sensors based on interdigitated electrodes integrated at the intermediate and proximal phalanges of an i-Limb. $\Delta V/V_0$ of all the capacitive sensors placed at B,C) proximal and D,E) intermediate phalanges, measured over time for touch operation with a gloved hand.

printed circuit had option to read ten sensors from the intermediate and proximal phalanges of five fingers of the i-Limb. A further description of the circuit and interface for capacitive sensing is shown in Figure S11 (Supporting Information). To measure the capacitances, the charge in the capacitor is discharged completely and then a constant current (I_C) of 55 μA was pumped into each of the sensor through a switching interface for a fixed time Δt (100 ms). The output voltages (V) from each sensor were read through the switching interface and a 10 bit analog-to-digital convertor interface of a microchip PIC (18F4X) microcontroller. A change in the output voltage because of the constant current pumped into the capacitive sensors is given by ΔV . Since I_C is pumped here for a small time, by measuring the change in the voltage the capacitance can be calculated by

$$C = I_C \left(\frac{\Delta V}{\Delta t} \right)^{-1} \quad (2)$$

Before measuring the capacitance, the voltage at each sensor was set to 0 V. The value of base voltage depends on the capacitance (sensitive to the sensor size, Figure 5A). Any change in capacitance will result in further modulation in the charged voltage compared to the base voltage that is denoted as $\Delta V/V_0$, which is plotted for sensors on various phalanges in Figure 5B,D with respect to time of touch operation with a gloved hand (see Movie S1 in the Supporting Information).

The charge time measurement is carried out sequentially for all the capacitive sensors by switching the channel shown in Figure S11 (Supporting Information) through the microcontroller. The data are acquired and sent to a PC serially, where a LabVIEW interface has been implemented for further processing, display, and analysis. The $\Delta V/V_0$ for proximal and intermediate phalanges are shown in Figure 5C,E, respectively. For proximal phalanges, the tactile input through a gloved hand caused a change in capacitance of 60%–140%, whereas for intermediate phalanges the change was from 30%–50% (in both cases including the experimental error). This observation is mainly because the active area of intermediate phalanges sensors is smaller ($8 \times 11 \text{ mm}^2$) than proximal phalanges for all the fingers (proximal sensors at heart (#3), index (#4), and thumb (#5) fingers have a size of $7 \times 20 \text{ mm}^2$, whereas at little (#1) and ring (#2) fingers they have a size of $7 \times 15 \text{ mm}^2$) hence the difference. It is worth noticing that the small difference in the active area of sensors is still detectable within proximal phalanges, observing higher modulation in proximal phalanges #3, #4, and #5 than proximal phalanges #1 and #2 (Figure 5C).

The viability of graphene-based skin sensors was also analyzed by means of a dynamic characterization consisting in the grabbing of a soft object as shown in Figure 6A. In this scenario, the readout interface circuitry allows us to measure the response of all sensors in contact with the object. Depending on the sensors active area covered with the object, we observed different changes of the readout voltages measured at each

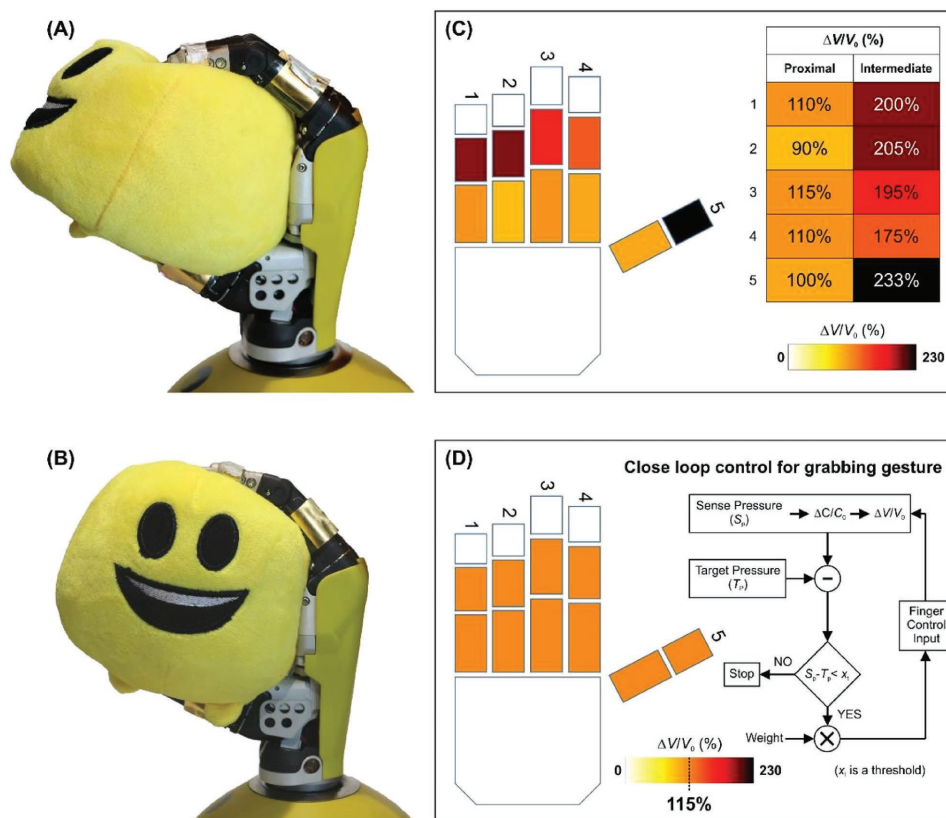


Figure 6. Dynamic characterization of a graphene touch sensor: “grabbing”. Grabbing of a soft ball A) disabling or B) enabling tactile feedback. Color map of the capacitive sensors, showing the readout voltage modulation after grabbing with tactile feedback C) disable or D) enable. Inset of (D) shows a logic diagram used to control grabbing of the hand with respect to the sensor readout.

sensor. Figure 6B shows a color map of the resultant grabbing experiment, obtaining variations between each sensor placed at different phalanges. Due to the morphology of the used soft object, sensors at intermediate phalanges show higher $\Delta V/V_0$ (up to 233% in the case of the thumb) than those obtained in the proximal ones. In addition, we measured the $\Delta C/C_0$ of each sensor during grabbing of a soft ball with the tactile feedback disable (i.e., under conditions of Figure 6A,C) to demonstrate the sensitivity of the sensors. Values of $\Delta C/C_0$ above 60% were observed, which correspond to a sensitivity of the sensor of 7.7 Pa^{-1} for pressures above 60 kPa. In this case, an increase of the touch sensor sensitivity at high pressures is beneficial for accurate response of the robotic motion in a wide range of pressures. That is good evidence of the touch/pressure detection capability of our graphene sensors under the routine bending situation, and a demonstration of potential application in robotics and prosthetics.

2.5. Grabbing of Objects Using Tactile Feedback

To further exploit the potential of these sensors, we have developed a close-loop system where the sensors are used to control the motion of the robotic hand. Figure 6A,B shows the grab of a soft ball having tactile feedback disable and enable, respectively. Comparing both figures, the latter shows a gentler grabbing of the soft object. This became possible because the movement of the hand was programmed in such a way that sensors placed at the phalanges received a maximum $\Delta V/V_0$ of 115%, as represented in Figure 6D. Following the logic diagram presented in the inset of Figure 6D, one can deduce that the grabbing motion of each finger is stopped when the $\Delta V/V_0$ overcomes a threshold value (in this case 115%). In this regard, sense pressure (S_p) of each finger is first measured through $\Delta C/C_0$ (or $\Delta V/V_0$) through the described sensor calibration (Figure 4E). Thereafter, the difference between S_p and the target pressure (T_p), i.e., $S_p - T_p$, is compared with a threshold value (x_t). On the one hand, a negative result stops the finger grabbing, indicating that the finger is applying the desirable pressure (see Movie 2 in the Supporting Information). On the other hand, if a positive result is obtained, first the resultant difference is weighted by a compliance parameter and then the finger control input will move the finger accordingly to the difference between the S_p and T_p . For example, at the beginning, fingers will grab the object very fast due to the high difference between S_p and T_p . In contrast, the finger grabbing will become slow when the difference between S_p and T_p is reduced, i.e., the object is almost grabbed using the desirable pressure. Here, we have demonstrated the potential of using a commercial off-the-shelf chip for reading out the transparent touch/pressure sensors response, making the grabbing of robotic fingers more accurate by mimicking human grabbing features.

2.6. Toward Energy Autonomy of e-Skin

Transparency of all the layers used in our touch sensor, including the protective layer (PDMS), the capacitive layer (graphene), and the flexible substrate (PVC), was used by

integrating the graphene touch sensors directly on top of solar cells. The effective integration of both technologies could, in future, allow the charging of batteries, either to power actuators or to power-up integrated circuits (ICs) on large area e-skin, leading to self-powered robotics/prosthetic limbs with tactile sensitivity. Accordingly, we fabricated a heterogeneous-layered-tactile-skin stack, comprising of photovoltaics in a back plane covered with a transparent e-skin layer based on graphene touch sensors. This is schematically illustrated in Figure 7A, where a transparent touch capacitive sensor is directly placed atop a solar cell. The transparent touch sensors consist of a PDMS protective layer on top of single-layer, graphene-based coplanar interdigitated electrodes with Ti/Au pads, and atop a flexible PVC substrate. Due to the intrinsic transparency of all layers existing in the sensor, incident light is expected to be efficiently transmitted through the whole structure (as shown in Figure 7A) reaching the surface of the solar cell. To demonstrate the viability of our approach, we first analyzed the optical transmission of graphene-based touch sensors. Figure 7B presents transmittance (T) and reflectance (R) measurements of graphene-on-PVC and 125- μm -thick PVC as a reference substrate. The measurements were carried out using a Shimadzu 2600 spectrophotometer. In our case, graphene-on-PVC shows a change in the T and R with respect to a PVC reference sample, ranging between 0.75%–2.75% and 0.3%–0.5%, respectively, going from 350 to 1000 nm wavelengths. This deviation is associated with the substrate effect during both transmittance and reflectance measurements throughout the broad wavelength range. The absorbance (A) of the single-layer graphene, removing the contribution from the PVC substrate, was calculated using the Beer–Lambert law, i.e., $A = \log_{10}(1/T)$, resulting in A ranged between 1.75% and 3.25% at wavelengths ranged between 400 and 1000 nm. The theoretical absorbance in the visible range of free-standing graphene is estimated around 2.3%;^[15] graphene samples studied in this work show A around 2.25%–2.50% at wavelengths ranged between 390 and 700 nm (visible spectrum), which means our touch sensors are based on single-layer graphene.

Figure 7C shows a photograph of an amorphous Si (a-Si) based solar cell (Sanyo Company), with an effective area of $39.6 \times 22.9 \text{ mm}^2$. The current–voltage (I – V) characteristics of this solar cell were measured after integration of different layers atop of its surface, including a graphene-on-PVC (Figure 7D), patterned graphene-on-PVC (Figure 7E), and patterned graphene-on-PVC encapsulated with PDMS (Figure 7F). Figure 7G summarizes the I – V characteristics obtained from each sample. Open circuit voltage (V_{oc}) and short circuit current (I_{sc}) of the solar cell were estimated from the interception of the curve with the x -axis and y -axis, respectively, as clearly observed in the inset of Figure 7G. We observed that both V_{oc} and I_{sc} parameters decrease as we add a layer on top of the solar cell surface, which means the graphene touch sensor is absorbing/reflecting partially the incident light. Some light may get scattered as well within the graphene touch sensor and interface before reaching the solar cell. From the power–voltage (P – V) characteristics of the solar cell (Figure 7H), we deduce a maximum power of around 1.48 mW with a maximum voltage (V_{pmax}) of 1.55 V and maximum current (I_{pmax}) of -0.95 mA . The integration of the touch sensor atop the solar cell could

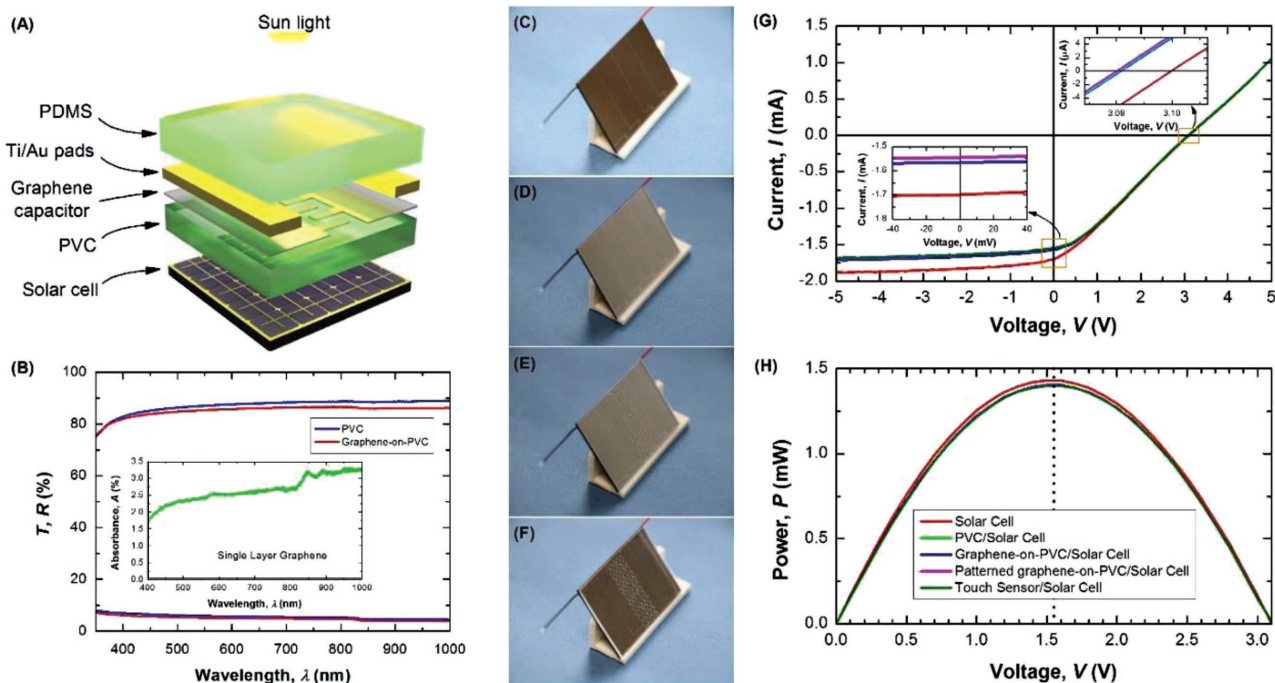


Figure 7. Heterogeneous integration of graphene transparent touch sensors atop a solar cell. A) 3D schematic illustration of the heterogeneous integration of a graphene touch sensor on top of a solar cell. B) Transmittance (T) and reflectance (R) spectra of single-layer graphene-on-PVC and a PVC reference substrate; inset: absorbance of single-layer graphene. Photograph of C) solar cell, D) graphene-on-PVC/solar cell, E) patterned graphene-on-PVC/solar cell, and F) graphene touch sensor/solar cell. G) I - V and H) P - V characteristics of the solar cell after integration of samples consisting of PVC, graphene-on-PVC, and graphene-on-PVC with a PDMS protective layer.

change the solar cell absorption performance. To analyze this effect, we studied the fill factor (FF) of the solar cell before and after integration of graphene touch sensors atop the solar cell surface. Prior to the graphene touch sensor integration, FF of the solar cell was 0.281, calculated by

$$FF = \frac{I_{pmax} V_{pmax}}{I_{sc} V_{oc}} \quad (3)$$

The integration of the graphene capacitive touch sensor atop the solar cell causes a decrease of the FF of around 8% (see Movie S3 in the Supporting Information).

The solar cell used in this work can produce a power of $160 \mu\text{W cm}^{-2}$. If the tactile skin presented here were to cover the glabrous skin of a human hand (average area around 120 cm^2), the solar cells used in this work would generate 19.2 mW , which is more than the power needed to drive an e-skin module, i.e., a graphene touch sensor. Further advancements in terms of high-efficiency energy-harvesting, energy-storing, and tetherless implementation could lead to a full autonomy of the e-skin. With a solar cell having better performance in an outdoor ambient environment than the one used here, we can generate much higher net power. For example, for the same hand area, a solar cell based on multicrystalline-Si (20.6 mW cm^{-2}), crystalline-Si ($\approx 26.3 \text{ mW cm}^{-2}$, Kaneka, rear junction), crystalline-Si ($\approx 25 \text{ mW cm}^{-2}$, UNSW-PERC), heterojunction with intrinsically thin ($\approx 25 \text{ mW cm}^{-2}$, Sanyo), and five-junction cell (38.8 mW cm^{-2} , Spectrolab) can result in a net power of around 2.5, 3.2, 3.0, 3.0, and 4.7 W , respectively.^[43]

The higher net power could either be stored for later use or used to drive the actuators of a robotic hand. However, some of the efficiency reported is on cell level and for module level it is expected to be lower.

To demonstrate the viability of our approach, we further designed a DC to AC circuit (Figure S12, Supporting Information) to transform the DC signal generated by 3 PV cells connected in parallel (output voltage: 2.6 V ; output current: 0.78 mA) into an AC signal ($V_{pp} = 1.2 \text{ V}$ and $f = 100 \text{ kHz}$). This was applied to the capacitive touch sensor module integrated on top of the PV cell. The frequency of the AC signal was chosen as per the capacitive region of the graphene touch sensors using impedance measurements (see Figure S13, Supporting Information). The designed circuit consumes a power of around 0.36 mW , which can be driven by the energy generated from PV cells (2.03 mW). With the generated AC signal applied to the touch sensor, the measured current before and during touching was 138 and 240 nA , respectively. This means the current increases due to the increase of the sensor capacitance around 10 pF during touching (see Movie S4 in the Supporting Information). The sensor consumes only 31 and 55 nW energy before and during the touching, respectively, which confirms the low power consumption of the capacitive touch sensors presented here. The effect of the blocking of light during touching on the solar cell energy generation was also analyzed by measuring the amplitude and frequency of the AC signal using an oscilloscope, and it was observed to have a low effect on the resulting output. This new concept is a step forward toward a new generation of energy-autonomous tactile skins by

harvesting ambient light energy to power up sensor-transducer ICs or a robotic hand's actuators. This approach can be further exploited by integrating our flexible touch sensors on flexible and stretchable solar cells, enabling a new concept of stretchable, energy-autonomous robotics and prosthetic skin.^[44]

3. Conclusions

This work presents a promising approach toward the development of an energy-autonomous, flexible, and transparent tactile skin based on single-layer graphene integrated onto a PV cell. Here, we demonstrated coplanar interdigitated electrodes based on single-layer graphene as transparent touch sensors. These sensors were realized by using a low cost, dry processing technique involving transfer printing of graphene on flexible substrates, and an electronic cutting tool to shape interdigitated electrodes on single-layer graphene. The dry method used here will enable rapid, large-area, and low-cost production of micrometric patterns in graphene, while preserving its properties and at the same time preventing the use of more complex, harmful, and often costly techniques, such as optical lithography and laser cutting. The combination of a PDMS protective layer and single-layer graphene coplanar capacitors is reported here for the first time. This structure makes the sensor highly sensitive over a wide range of pressures, as the sensors could detect pressures up to 80 kPa and minimum pressures of 0.11 kPa with a sensitivity of 4.3 Pa⁻¹. As a potential application of the presented transparent tactile skin, we demonstrated the integration of touch sensors on the phalanges of a bionic hand and used the touch feedback to grab soft objects in a controlled way. Furthermore, due to the significant transparency of these sensors and their low power consumption, we demonstrated a promising alternative to replace the battery with a solar cell in the back plane of the touch sensors, leading to a new concept of energy-autonomous tactile skins for robotics, prosthetics, and wearable systems.

4. Experimental Section

Transfer of Single-Layer Graphene on a PVC Flexible Substrate: 4 in. CVD monolayer graphene on Cu (Graphenea) in this work was laminated on 125- μ m-thick PVC substrates (Fellowes gloss laminating pouch) using a hot-lamination method at 125 °C (Fellowes Saturn 3i(A4)). Cu side was placed in contact with a paper, whereas graphene side was directly contacted with the PVC, resulting in the structure PVC/graphene/Cu/paper/PVC. The use of paper prevents the lamination of copper on PVC, being only the graphene side laminated on the PVC surface. After lamination, copper was etched using a 1 M FeCl₃ in deionized water etching solution for 2 h; this reaction can be speeded up by heating the etching solution up to 50 °C, resulting in a shorter etching period of about 30 min.

Characterization of Single-Layer Graphene on a PVC Flexible Substrate: Sheet resistance of graphene was analyzed by the TLM. Ti (10 nm)/Au (100 nm) electrodes were directly evaporated on the edges of the graphene-on-PVC samples in an e-beam evaporator with a background pressure of 10⁻⁵ Pa. Channels with a width of $W_c = 11$ mm and lengths of $L_c = 2.5$ –33 mm were defined using a polymer shadow mask on graphene area.

Fabrication of a Touch Sensitive Layer: Once graphene was transferred onto the PVC substrate, interdigitated electrodes were shaped using a

blade-cutting system (Silhouette Cameo). Prior to the cutting, samples were attached to a cutting mat making the procedure more accurate. Silhouette software allows controlling various parameters, including the blade height, cutting thickness, and cutting speed. In addition, the software has a library with a wide selection of standard materials. For shaping the electrodes in graphene, the minimum ratchet blade position of 0, a cutting thickness position of 1, and a cutting speed of 1 cm s⁻¹ were used. These conditions were demonstrated not to damage graphene, creating a sharp edge at the cutting gap and preserving graphene structure elsewhere.

Transmission Spectroscopy Characterization of e-Skin: The characterization of optical transmission of touch sensors under light illumination was carried out using a UV-vis spectrophotometer (Shimadzu-2600). Optical absorption of single-layer graphene laminated on PVC was analyzed by measuring T and R of samples for light wavelengths ranging between 350 and 1000 nm. To subtract the contribution of the substrate, a reference sample was used, consisting of a laminated PVC substrate without graphene.

Supporting Information

Supporting Information is available from the Wiley Online Library or from the author.

Acknowledgements

This work was supported in part by the European Commission under Grant Agreements PITN-GA-2012-317488-CONTEST, EPSRC Engineering Fellowship for Growth – PRINTSKIN (EP/M002527/1), and EPSRC First Grant (EP/M002519/1). The authors are thankful to the support received for this work from James Watt Nanofabrication Centre (JWNC) and Electronics Systems Design Centre (ESDC).

Received: November 29, 2016

Revised: February 13, 2017

Published online: March 22, 2017

- [1] N. Yogeswaran, W. Dang, W. T. Navaraj, D. Shakthivel, S. Khan, E. O. Polat, S. Gupta, H. Heidari, M. Kaboli, L. Lorenzelli, *Adv. Robotics* **2015**, *29*, 1359.
- [2] B. C. K. Tee, C. Wang, R. Allen, Z. N. Bao, *Nat. Nanotechnol.* **2012**, *7*, 825.
- [3] S. Bauer, *Nat. Mater.* **2013**, *12*, 871.
- [4] C. Wang, D. Hwang, Z. Yu, K. Takei, J. Park, T. Chen, B. Ma, A. Javey, *Nat. Mater.* **2013**, *12*, 899.
- [5] J. J. Boland, *Nat. Mater.* **2010**, *9*, 790.
- [6] R. S. Dahiya, P. Mittendorfer, M. Valle, G. Cheng, V. J. Lumelsky, *IEEE Sens. J.* **2013**, *13*, 4121.
- [7] R. S. Dahiya, G. Metta, M. Valle, G. Sandini, *IEEE Trans. Robotics* **2010**, *26*, 1.
- [8] R. Dahiya, W. Navaraj, S. Khan, E. O. Polat, *Inf. Disp.* **2015**, *31*, 6.
- [9] D. J. Lipomi, B. C. K. Tee, M. Vosgueritchian, Z. Bao, *Adv. Mater.* **2011**, *23*, 1771.
- [10] Y. J. Wei, B. L. Wang, J. T. Wu, R. G. Yang, M. L. Dunn, *Nano Lett.* **2013**, *13*, 26.
- [11] M. G. Rybin, A. S. Pozharov, E. D. Obraztsova, *Phys. Status Solidi C* **2010**, *7*, 2785.
- [12] S. Stankovich, D. A. Dikin, G. H. B. Dommett, K. M. Kohlhaas, E. J. Zimney, E. A. Stach, R. D. Piner, S. T. Nguyen, R. S. Ruoff, *Nature* **2006**, *442*, 282.
- [13] X. Wang, L. J. Zhi, K. Mullen, *Nano Lett.* **2008**, *8*, 323.

- [14] X. S. Li, Y. W. Zhu, W. W. Cai, M. Borysiak, B. Y. Han, D. Chen, R. D. Piner, L. Colombo, R. S. Ruoff, *Nano Lett.* **2009**, *9*, 4359.
- [15] E. O. Polat, O. Balci, N. Kakenov, H. B. Uzlu, C. Kocabas, R. Dahiya, *Sci. Rep.* **2015**, *5*, 16744.
- [16] M. S. Lee, K. Lee, S. Y. Kim, H. Lee, J. Park, K. H. Choi, H. K. Kim, D. G. Kim, D. Y. Lee, S. Nam, J. U. Park, *Nano Lett.* **2013**, *13*, 2814.
- [17] Y.-M. Chen, S.-M. He, C.-H. Huang, C.-C. Huang, W.-P. Shih, C.-L. Chu, J. Kong, J. Li, C.-Y. Su, *Nanoscale* **2016**, *8*, 3555.
- [18] C. Metzger, E. Fleisch, J. Meyer, M. Dansachmüller, I. Graz, M. Kaltenbrunner, C. Keplinger, R. Schwödiauer, S. Bauer, *Appl. Phys. Lett.* **2008**, *92*, 013506.
- [19] S. C. B. Mannsfeld, B. C. K. Tee, R. M. Stoltenberg, C. V. H. H. Chen, S. Barman, B. V. O. Muir, A. N. Sokolov, C. Reese, Z. N. Bao, *Nat. Mater.* **2010**, *9*, 859.
- [20] D. H. Ho, Q. Sun, S. Y. Kim, J. T. Han, D. H. Kim, J. H. Cho, *Adv. Mater.* **2016**, *28*, 2601.
- [21] A. Shirinov, W. Schomburg, *Sens. Actuators, A* **2008**, *142*, 48.
- [22] H. B. Yao, J. Ge, C. F. Wang, X. Wang, W. Hu, Z. J. Zheng, Y. Ni, S. H. Yu, *Adv. Mater.* **2013**, *25*, 6692.
- [23] H. Tian, Y. Shu, X.-F. Wang, M. A. Mohammad, Z. Bie, Q.-Y. Xie, C. Li, W.-T. Mi, Y. Yang, T.-L. Ren, *Sci. Rep.* **2015**, *5*, 8603.
- [24] V. Mosser, J. Suski, J. Goss, E. Obermeier, *Sens. Actuators, A* **1991**, *28*, 113.
- [25] R. R. Spender, B. M. Fleischer, P. W. Barth, J. B. Angell, *IEEE Trans. Electron Devices* **1988**, *35*, 1289.
- [26] G. Schwartz, B. C. K. Tee, J. G. Mei, A. L. Appleton, D. H. Kim, H. L. Wang, Z. N. Bao, *Nat. Commun.* **2013**, *4*, 1859.
- [27] K. Takei, T. Takahashi, J. C. Ho, H. Ko, A. G. Gillies, P. W. Leu, R. S. Fearing, A. Javey, *Nat. Mater.* **2010**, *9*, 821.
- [28] T. Someya, T. Sekitani, S. Iba, Y. Kato, H. Kawaguchi, T. Sakurai, *Proc. Natl. Acad. Sci. USA* **2004**, *101*, 9966.
- [29] B. W. Zhu, Z. Q. Niu, H. Wang, W. R. Leow, H. Wang, Y. G. Li, L. Y. Zheng, J. Wei, F. W. Huo, X. D. Chen, *Small* **2014**, *10*, 3625.
- [30] R. S. Dahiya, M. Valle, *Robotic Tactile Sensing: Technologies and System*, Springer Science & Business Media, Dordrecht **2013**.
- [31] L. G. Martins, Y. Song, T. Zeng, M. S. Dresselhaus, J. Kong, P. T. Araujo, *Proc. Natl. Acad. Sci. USA* **2013**, *110*, 17762.
- [32] G. Radhakrishnan, J. D. Cardema, P. M. Adams, H. I. Kim, B. Foran, *J. Electrochem. Soc.* **2012**, *159*, A752.
- [33] D. Wei, S. Haque, P. Andrew, J. Kivioja, T. Ryhanen, A. Pesquera, A. Centeno, B. Alonso, A. Chuvilin, A. Zurutuza, *J. Mater. Chem. A* **2013**, *1*, 3177.
- [34] X. Li, W. Cai, J. An, S. Kim, J. Nah, D. Yang, R. Piner, A. Velamakanni, I. Jung, E. Tutuc, S. K. Banerjee, L. Colombo, R. S. Ruoff, *Science* **2009**, *324*, 1312.
- [35] Z. Suo, E. Y. Ma, H. Gleskova, S. Wagner, *Appl. Phys. Lett.* **1999**, *74*, 1177.
- [36] S. Bae, H. Kim, Y. Lee, X. Xu, J.-S. Park, Y. Zheng, J. Balakrishnan, T. Lei, H. Ri Kim, Y. I. Song, Y.-J. Kim, K. S. Kim, B. Ozyilmaz, J.-H. Ahn, B. H. Hong, S. Iijima, *Nat. Nanotechnol.* **2010**, *5*, 574.
- [37] X. Liang, Z. Fu, S. Y. Chou, *Nano Lett.* **2007**, *7*, 3840.
- [38] Y. Zhou, K. P. Loh, *Adv. Mater.* **2010**, *22*, 3615.
- [39] Y. Zhou, Q. Bao, B. Varghese, L. A. L. Tang, C. K. Tan, C. H. Sow, K. P. Loh, *Adv. Mater.* **2010**, *22*, 67.
- [40] R. Sahin, E. Simsek, S. Akturk, *Appl. Phys. Lett.* **2014**, *104*, 053118.
- [41] M. W. Toepke, D. J. Beebe, *Lab Chip* **2006**, *6*, 1484.
- [42] E. Baltussen, P. Sandra, F. David, C. Cramers, *J. Microcolumn Sep.* **1999**, *11*, 737.
- [43] M. A. Green, K. Emery, Y. Hishikawa, W. Warta, E. D. Dunlop, D. H. Levi, A. W. Y. Ho-Baillie, *Prog. Photovolt.: Res. Appl.* **2017**, *25*, 3.
- [44] W. Dang, V. Vinciguerra, L. Lorenzelli, R. Dahiya, *Flex. Print. Electron.* **2017**, at press: <https://doi.org/10.1088/2058-8585/aa5ab2>.